The NA50 segmented target and vertex recognition system

F. Bellaiche, B. Cheynis, D. Contardo, O. Drapier, J.Y. Grossiord [1], A. Guichard, R. Haroutunian, M. Jacquin, F. Ohlsson-Malek, J.R. Pizzi

Institut de Physique Nucléaire de Lyon, IN2P3-CNRS et Université Claude Bernard Lyon-I, France

The NA50 segmented target and vertex recognition system is described. The segmented target consists of 7 sub-targets of 1-2 mm thickness. The vertex recognition system used to determine the sub-target where an interaction has occured is based upon quartz elements which produce Čerenkov light when traversed by charged particles from the interaction. The geometrical arrangement of the quartz elements has been optimized for vertex recognition in ^{208}Pb-Pb collisions at 158 GeV/nucleon. A simple algorithm provides a vertex recognition efficiency of better than 85% for dimuon trigger events collected with a 1 mm sub-target set-up. A method for recognizing interactions of projectile fragments (nuclei and/or groups of nucleons) is presented. The segmented target allows a large target thickness which together with a high beam intensity ($\approx 10^7$ ions/s) enables high statistics measurements.

[1] Corresponding author

Preprint submitted to Elsevier Preprint *20 February 1997*

1 Introduction

The CERN experimental program dedicated to the search for Quark-Gluon Plasma (QGP) began in 1986 with the 200 GeV/nucleon ^{16}O and ^{32}S beams and has been extended since 1994 to the 158 GeV/nucleon ^{208}Pb beam. Among the various experiments devoted to this field of physics, the NA38 [1–3] followed by the NA50 [4] experiment is dedicated to the detection of dimuons, mainly from the decay of the vector meson resonances ρ, ω, ϕ, J/ψ, and ψ', the Drell-Yan (DY) process, and the semi-leptonic decay of the charmed mesons D$\bar{\mathrm{D}}$. The dimuon kinematical variables are measured with the NA10 spectrometer [5]. Information on the collision geometry and the energy dissipated by the two interacting ions is obtained from the measurement of the neutral transverse energy $\mathrm{E_T}$ (NA38 and NA50), the multiplicity of charged particles $\mathrm{M_{CH}}$ (NA50) [6], and the forward residual hadronic energy $\mathrm{E_{ZDC}}$ (NA50).

High mass dimuon production has a very low cross-section in nucleon-nucleon interactions (e.g. $\sigma_{\mathrm{pp}}^{\mathrm{J}/\psi\to\mu^+\mu^-} \approx$2 nb) and in nucleus-nucleus reactions in spite of a multiplicative scaling factor close to $\mathrm{A_{proj.}.A_{targ.}}$ [3]. It is therefore necessary to use, in addition to a high beam intensity, a thick target. In order to minimize interactions of the produced particles inside this thick target, which would corrupt the information from observables such as $\mathrm{E_T}$, $\mathrm{M_{CH}}$, $\mathrm{E_{ZDC}}$, ..., correlated with the dimuon production, a segmented target with small transverse dimension is used. Consequently, the segmented target must be equipped with detection devices to allow the determination of the sub-target primary vertex where the interaction has occured. This is needed to improve the dimuon mass calculation and other measurements (e.g. $\mathrm{E_T}$) requiring determination of the detection geometry. In addition, the detection devices should identify interactions of projectile fragments in the downstream target elements.

The vertex determination in the NA38 experiment (^{16}O-U and ^{32}S-U collisions) has been made by scintillator hodoscopes used to measure charged particles, including target evaporation products, emitted in the collisions. The description and the performance of the method can be found in references [1,7]. The adaptation of this technique to the NA50 experiment (^{208}Pb-Pb collisions) encountered two difficulties. First, the high radiation level in the target vicinity (36 Mrad/month with 10^7 Pb ions/s) made difficult the use of scintillator counters without damage. A device made of quartz elements producing Čerenkov light was therefore adopted. Secondly, as a consequence of the choice of Čerenkov light detection, only fast charged particles emitted from the collision were detectable, eliminating the possibility to detect slow target evaporation fragments. In order to optimize the vertex recognition efficiency, a device made of counters very close to the beam axis and with a geometry which took advantage of the angular properties of the Čerenkov light was chosen.

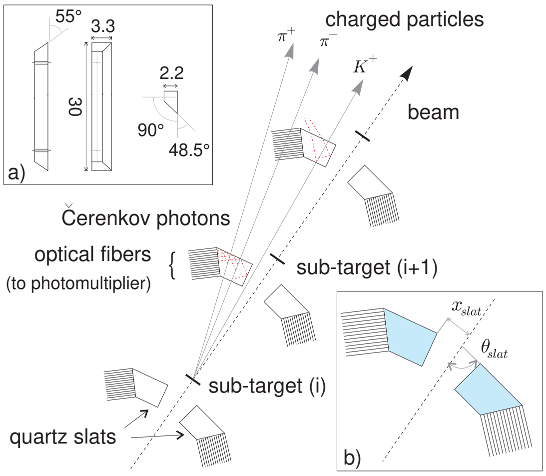

Fig. 1. Horizontal cut view of a section of the NA50 segmented target, a) geometrical shape of the quartz slat (dimensions in mm), b) parameters of the slats relative to the beam axis. See text Section 2.1.

After describing the device for the determination of the vertex (Section 2), and its optimisation (Section 3), we give its performance in terms of precision and efficiency (Section 4) for ^{208}Pb-Pb interactions with associated dimuon detection. A method for identification of heavy fragment interactions is presented and applied to the NA50 data (Section 5). A more detailed presentation can be found in Reference [8].

2 Description of the system

2.1 Principle

The vertex recognition within the segmented target makes use of a row of slats made of quartz located on both left and right sides of the sub-targets as shown in Fig. 1.

An interaction in sub-target i (vertex in i) produces charged particles which generate Čerenkov light in the downstream slats. The angular properties of the emitted light lead to a pattern of slat signals which allows to identify the vertex sub-target (see Fig. 1). The slat angle relative to the beam axis is such that each vertex slat i (the left and right slats immediately downstream of the sub-target i), transmits light, by total reflection on the two parallel faces, to its associated photomultiplier while for downstream slats j>i (left and right), the light is mainly refracted and lost. This geometrical arrangement is such that the collected light amplitude decreases when the slat index increases, although the charged particle multiplicity through each slat element increases. This geometrical effect is optimized experimentally (see Section 3). It is an important criterion to obtain a large efficiency to recognize the vertex and to identify fragment interactions.

2.2 Geometry and simulation

The target built for the NA50 experiment has the possibility to accomodate a maximum of 7 sub-targets individually insertable, each 1-2 mm thick, corresponding to 2.5-5.0% of an interaction length (λ_i). Their transverse section is circular with a diameter of 2.5 mm, except for the first sub-target which is larger (5 mm) in order to intercept the full beam for a correct luminosity measurement [8]. The sub-targets are placed at 25 mm intervals along the beam axis. Each sub-target is followed 20 mm downstream by two slats located slightly off the beam axis. Their shape and dimensions are given in Fig. 1. The angular range projected onto the median horizontal plane is about 150 mrad. The angle θ_slat and distance x_slat of the slats in each row relative to the beam axis are remotly adjustable, from the counting room, by the use of independent mechanical translation and rotation devices.

The response of the system has been simulated with minimum bias Pb-Pb interactions using the FRITIOF code [9] to generate events and the GEANT code [10] to simulate δ-ray production, particle interactions, and Čerenkov light tracking. A slat inclination angle $\theta_\mathrm{slat} = 76°$ and a distance $x_\mathrm{slat} = 2.5$ mm relative to the beam axis have been chosen as optimal. This configuration corresponds to an angular range of 125-280 mrad (a pseudo-rapidity range of 2.77-1.96) in the horizontal beam plane. The sub-target thickness was 1 mm, and only the left half of the system was simulated. The collisions took place in sub-target 2 with a beam size characterized by $\sigma_\mathrm{x} = \sigma_\mathrm{y} = 0.4$ mm and $\sigma_\theta = \sigma_\phi = 0$ mrad.

The number of charged particles through the successive slats and the recorded slat signals are plotted in Fig. 2 as a function of the impact parameter of the Pb-Pb collision. The signals represent the number of photo-electrons extracted from the photocathodes (quantum efficiency 25%) after a light attenuation of 70% due to the fiber light guide. Photo-electron fluctuations were not included.

The distributions in Fig. 2a show that the number of charged particles through the slats is slightly increasing with the slat index (except for slat 1 which is upstream of the collisions). Meanwhile, the light collected from slat 2 (Fig. 2b) is larger that the light collected in the other downstream slats, showing clearly the expected geometrical effect despite a non-negligible angular spread of the particle tracks through the slats. We observe that the identification of the vertex in sub-target 2 (condition of the simulation) is possible with a simple threshold set above the signal delivered by the slat 1. Such a simple procedure

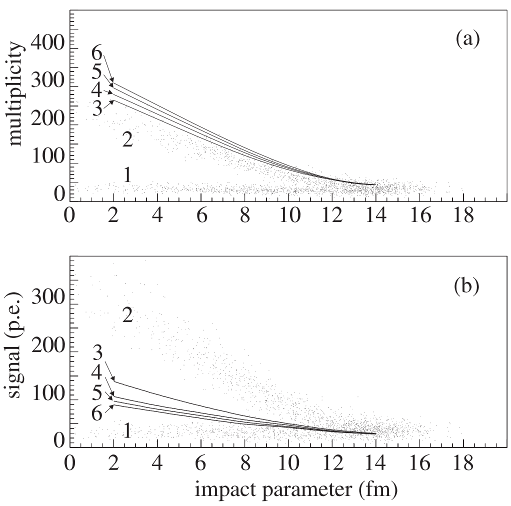

Fig. 2. Minimum bias Pb-Pb interactions generated with Fritiof in sub-target 2 (1000 events). Response of the left side of the NA50 segmented target simulated with the GEANT code. a) charged particle multiplicity (including δ-electrons) through the successive slats, b) number of photo-electrons collected by the corresponding slats, as a function of the impact parameter of the reaction. The points are the responses of the slats 1 and 2, the lines represent the mean responses of the slats i = 3-6. See text Section 2.2.

allows to reach a 100% efficiency for Pb-Pb collisions up to an impact parameter of 9 fm. Beyond this value, fluctuations of the signals make the efficiency lower.

2.3 Technical choices

The slats are made of silica of SUPRASIL I[2] quality. In order to obtain the best efficiency for light collection, propagation, and multiplication (the light wavelength covers the UV range 200-600 nm), we use radiation resistant "hard cladding" silica/silica/polyimide fiber (core/cladding/hard coat = 400/440/470 μm, numerical aperture = 0.22), without external sheath. Each light guide is made of 250 fiber bits[3]. This arrangement allows to transmit the light to XP2020Q[4] photomultipliers with quartz windows. Each slat/guide set is mounted on a thin aluminium holder (1 mm thick) in order to minimize interactions of secondary particles.

The construction of two rows of slats, instead of one, enables to require similar signals from left and right slats with the same index. This is very efficient to discriminate charged particle background impinging on not only the counters

[2] HERAEUS, Les Ulis, France.
[3] SEDI Fibres Optiques, Evry, France.
[4] PHILIPS PHOTONIQUE, Suresnes, France.

Fig. 3. The NA50 row of sub-targets with, in both side and in remote position, the quartz slats and the light guides for vertex recognition. The upstream antihalo counter is visible in the background (photo Guy Jacquet).

themselves but also the quartz windows of the photomultipliers which are a good medium for producing Čerenkov light. In order to reduce this source of background further, the manufacturer developed photomultipliers with an active photocathode area reduced by a factor of 5 (XP2020Q series M03).

A pair of additional slats (index 0), upstream of the two rows of slats dedicated to the vertex measurement, is used to recognize interactions occuring in air before the first sub-target. Furthermore, a pair of halo counters made of the same material as the slats (square of 40.40 mm^2 with thickness of 0.8 mm), with a hole in their center, allowed to eliminate incident ions outside a cylinder of 3 mm in diameter. This cylinder included practically the full beam which had dimensions of about $\sigma_x \approx \sigma_y \approx 0.4$ mm and $\sigma_\theta \approx \sigma_\phi \approx 0.25$ mrad. Fig. 3 shows a photograph of the system viewed from the downstream end.

3 Sensitivity optimization

The sensitivity of the vertex recognition system is a function of the geometrical position of the slats relative to the Čerenkov light emission angles inside the slats themselves. The optimization of the geometry is a compromise between a minimization of the signal ratio S_{i+1}/S_i and a maximization of the S_i value. S_i and S_{i+1} are the signals delivered by the photomultipliers associated with slats i and i+1, the index i being the vertex number.

In order to determine the best geometrical position of the slats in each row we measured the distributions of the quantities S_2/S_1 and S_1 as a function of θ_{slat} from 74° to 78°. The slat to beam axis distance was fixed at $x_{slat} = 2.5$ mm and only sub-target 1 was used to produce interactions. Fig. 4 shows the S_2/S_1

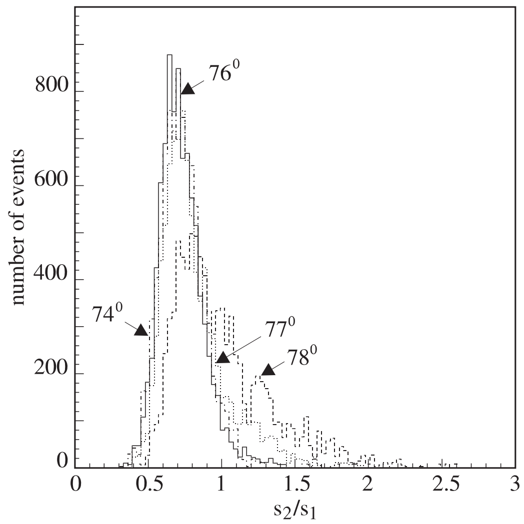

Fig. 4. Dimuon triggered Pb-Pb interactions in sub-target 1. Distributions of S_2/S_1, the ratio of the signals measured with the left slats 2 and 1, as a function of θ_{slat}. See text Section 3.

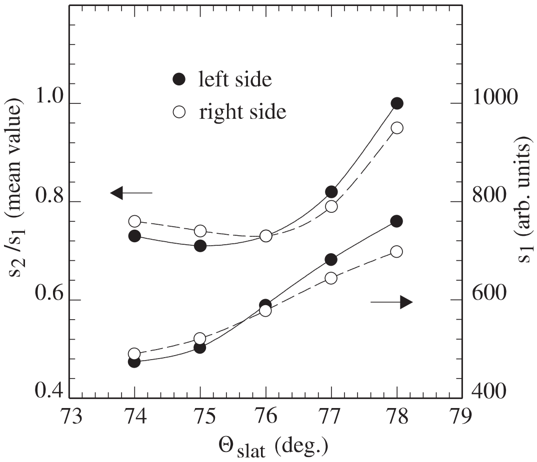

Fig. 5. Dimuon triggered Pb-Pb interactions in sub-target 1. S_2/S_1 mean values and S_1 signals as a function of θ_{slat}. See text Section 3.

distributions obtained with the left row. The distributions are clearly seen to become narrower with decreasing angle. At 76° and 74° they have similar symmetrical shapes with more than 95% of the peaks below 1.

The S_2/S_1 mean values and the S_1 signals are plotted in Fig. 5 for the left and right rows. It shows that a good compromise for the choice of θ_{slat} is 76°. Indeed, the S_2/S_1 mean values reach a minimum while the S_1 signals are still not too much attenuated. These geometrical conditions were adopted for the Pb-Pb data taking in 1995 and 1996.

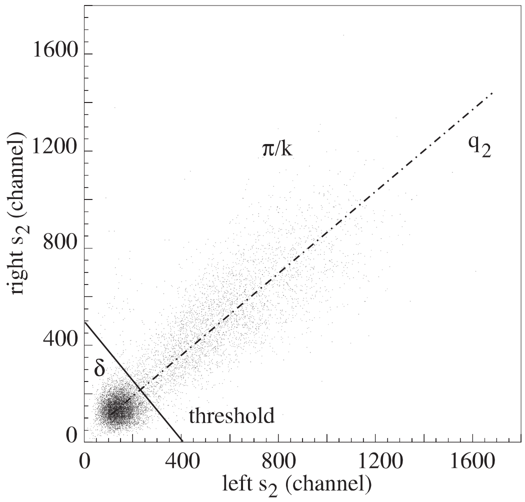

Fig. 6. Dimuon triggered Pb-Pb interactions in sub-targets 1-7. Left and right slat 2 correlated signals. See text Sections 4.1 and 5.1.

4 ^{208}Pb-Pb vertex identification

4.1 Algorithm

The beam crossing the sub-targets (and the air in the gaps) produces δ-electrons through electromagnetic processes. The electrons hitting the slats produce Čerenkov light which constitutes an unavoidable correlated background signal. Any nuclear interaction occuring in one of the seven sub-targets (or in the air) produces signals which add to the δ-electron background signal in the downstream slats, including the vertex slats.

The left and right correlated signals recorded from interactions triggered by dimuons are plotted in Fig. 6 for slats 2. The δ-electrons associated with interactions downstream of sub-target 2 are clearly observed as the intense cluster of events with small signals. The correlated band of events with increasing signals are due to π/K particles produced by interactions in sub-targets 1 and 2.

The vertex recognition algorithm is based on the systematic search, event by event, starting at slats 1 and ending at slats 7, for the sub-target with the first correlated signal which is above the δ signal threshold (see Fig. 6). This threshold was determined, for each pair of slats, using the corresponding two-dimensional distribution, similar to that shown in Fig. 6, for δ signals only. The δ signal distributions were obtained from Pb ion crossing the sub-target row without interacting.

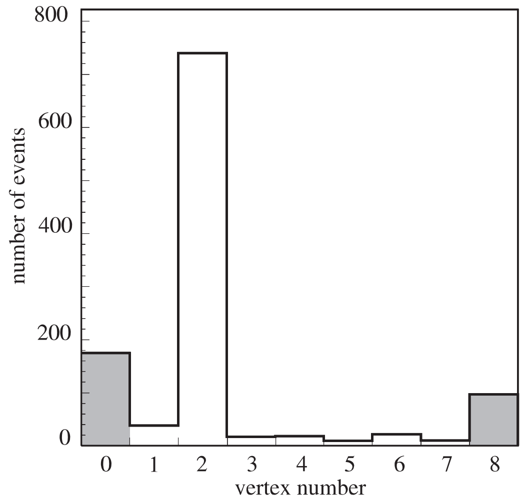

Fig. 7. Response of the algorithm for dimuon triggered Pb-Pb interactions in a 2 mm thick sub-target set in position 2. See text Section 4.2.

4.2 Single sub-target recognition efficiency

The performance of the vertex recognition algorithm applied to dimuon data recorded with a 2 mm thick sub-target alone in position 2 is illustrated in Fig. 7. Sub-target 2 is selected most frequently, as expected, with vertices 1 and 3-7 selected with a much lower frequency. Although the sub-targets are absent, the selection of the other vertices is largely a result of interactions of Pb with the 150 mm of air, representing 0.3% of an interaction length in the region of the slats. The relative contribution from air is decreased when all sub-targets are used. The events identified with vertex 0 indicate interactions which occur upstream of sub-target 1. Vertex 8 indicates those events in which no slat had the signal above the threshold. These events correspond to (very) peripheral nuclear interactions for which the vertex recognition system is inefficient.

The overall efficiency for identifying an interaction in any sub-target of the system is $N_{1-7}/N_{1-8} = 92\%$. The efficiency for identifying the correct sub-target is $N_2/N_{1-7} = 86\%$ which is probably an underestimate on account of the background from interactions in air. The efficiencies calculated above may be considered as intrinsic efficiencies of the system, characteristic of the single sub-target configuration.

4.3 Full sub-target efficiency

It must be stressed that the δ-electron contribution to the slat signals depends strongly on the configuration of the sub-targets (position and thickness). As a result, the slat thresholds and therefore vertex efficiencies depend strongly

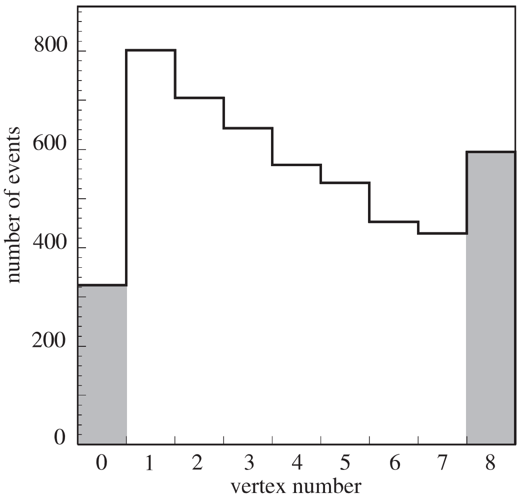

Fig. 8. Response of the algorithm for dimuon triggered Pb-Pb interactions in 7 sub-targets of 1 mm thickness. See text Section 4.3.

on the sub-target configuration. For example, in the single sub-target configuration the threshold values decrease with increasing index following the sub-target position. In the case where all the sub-targets are in the beam, the threshold values are an increasing function of the sub-target index, due to the cumulative δ contributions. In this case, the vertex recognition efficiency decreases with increasing sub-target index. Since the full sub-target configuration constitutes the usual data taking condition, it is important to know the performance of the system in this configuration.

For the full sub-target configuration (each 1 mm thick) the vertex determination of the dimuon triggered Pb-Pb interactions leads to the typical distribution shown in Fig. 8. The yield decreases from the vertex in sub-target 1 to the vertex in sub-target 7. The meaning of channels 0 and 8 is the same as described in Section 4.2. Except for a slight over-filling of vertex in sub-target 1, due to the larger transverse size intercepting the full beam, the decreasing pattern from vertex in sub-target 1 to vertex in sub-target 7 is the result of three incoherent effects. First, the incident beam quantity diminishes after each sub-target, due to interactions ($\lambda_i = 2.5\%$). Secondly, the muon pair background originating from π/K meson decays is a strong function of the distance between the vertex and the hadron absorber in front of the spectrometer [4]. This distance is 300 mm for a vertex in sub-target 1 and 150 mm for a vertex in sub-target 7. Thirdly, the vertex recognition efficiency decreases with increasing sub-target index as a result of the increasing threshold.

The overall vertex determination efficiency can be expressed by the general relation $\mathrm{eff}_{1-7}(X) = N_{1-7}(X)/N_{1-8}(X)$ where $N(X)$ is the distribution of some physical quantity measured from events with recognized (1-7) or not recognized (8) vertices. In particular, we would like to evaluate the efficiency as a function of the transverse energy E_T. This quantity is calculated from the for-

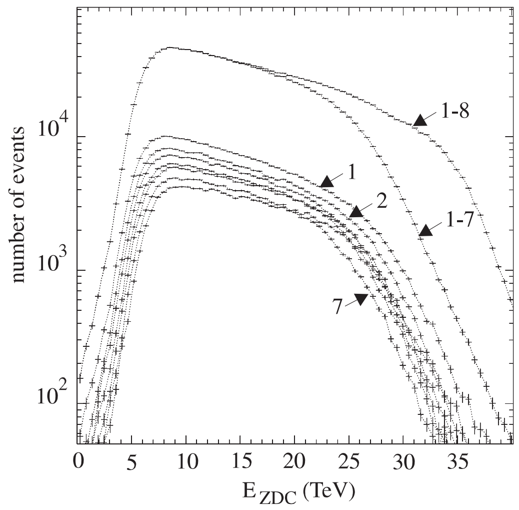

Fig. 9. Dimuon triggered Pb-Pb interactions in 7 sub-targets of 1 mm thickness. Distributions of remaining longitudinal energy E_{ZDC} for all events (1-8), for events with a recognized vertex (1-7) and for events associated with each vertex (1, 2, ..., 7). See text Section 4.3.

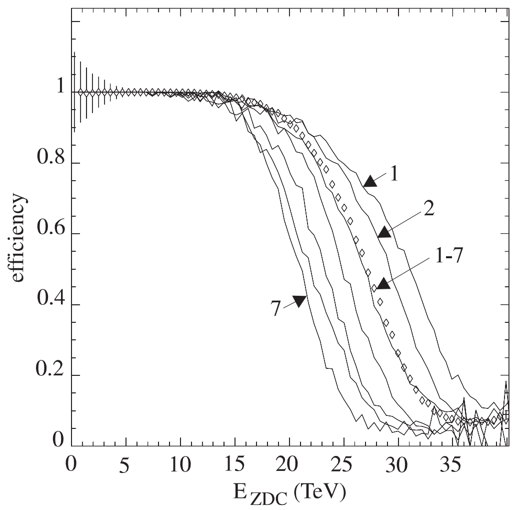

Fig. 10. Dimuon triggered Pb-Pb interactions in 7 sub-targets of 1 mm thickness. Vertex recognition efficiency versus E_{ZDC} for recognized vertex (1-7, diamond) and for events associated with each vertex (1, 2, ..., 7). See text Section 4.3.

mula $\sum_j E_j \sin\theta_j$ where E_j is the energy measured by element j of the calorimeter and θ_j is the mean angle under which this element is viewed. Thus the efficiency calculation as a function of E_T requires knowledge of the vertex for each event. This prevents using E_T for the efficiency measurement.

Instead, we evaluate the efficiency as a function of the remaining longitudinal energy E_{ZDC}. In this case, knowledge of the vertex is not necessary. The E_{ZDC} distribution for Pb-Pb interactions in coincidence with dimuons is shown in Fig. 9 for all events (1-8) and for events with recognized vertex (1-7). The

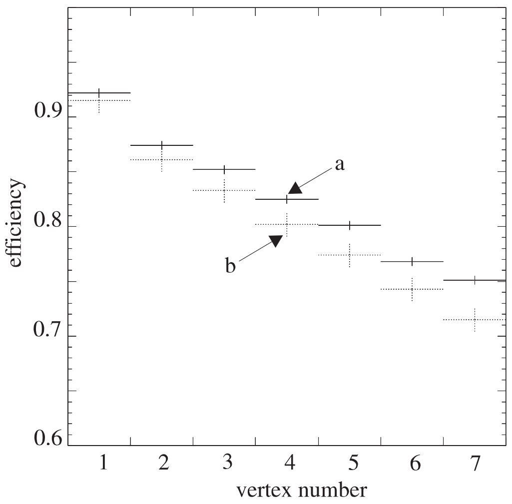

Fig. 11. Dimuon triggered Pb-Pb interactions. Vertex recognition efficiency versus the vertex number a) for sub-targets 1-7 of 1 mm thickness, b) for sub-targets 1, 7 of 1 mm thickness and sub-targets 2-6 of 2 mm thickness. See text Section 4.3.

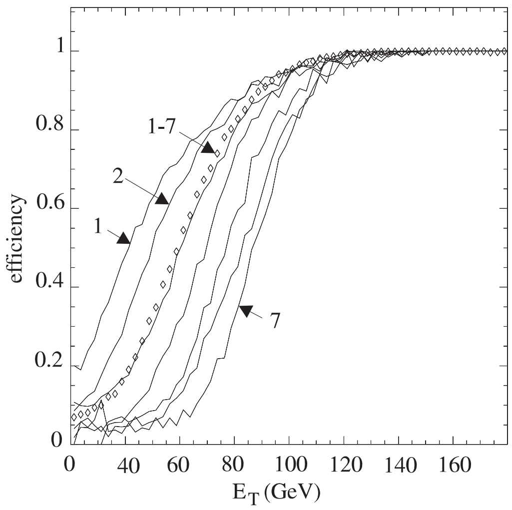

Fig. 12. Dimuon triggered Pb-Pb interactions in 7 sub-targets of 1 mm thickness. Vertex recognition efficiency versus E_T for recognized vertex (1-7, diamond) and for events associated with each vertex (1, 2, ..., 7). See text Section 4.3.

only difference of shape between the two distributions appears at large ZDC energies, corresponding to peripheral Pb-Pb collisions for which the vertex algorithm is not efficient.

The integrated efficiency $\mathrm{eff}_{1-7} = N_{1-7}/N_{1-8}$ is about 85%. Its distribution as a function of E_{ZDC} is shown in Fig. 10. As expected, eff_{1-7} increases when E_{ZDC} decreases. The efficiency is 1 for E_{ZDC} below 9 TeV with large error bars due to low statistics. We fixed it to 1, without incertainty, between 0 and 9 TeV, range which corresponds to the most central collisions. Furthermore, the fact that the eff_{1-7} value is 1 below around 9 TeV allows one to conclude that it is also 1 below around 9 TeV for the individual sub-targets. We then calculate a sub-target efficiency eff_i by dividing the corresponding E_{ZDC} distribution, correctly normalized in the region around 9 TeV, by the full E_{ZDC} distribution as shown in Fig. 9. The individual efficiency distributions are plotted in Fig. 10. They clearly show the effect of increasing threshold for large E_{ZDC} values. Their integrated values are plotted in Fig. 11 where the error bars represent the uncertainty on the normalisation factor between the full and individual distributions. Also plotted in the same figure are efficiency values for a thicker target configuration. The threshold effects are stronger and reduce the integrated efficiency to about 82%. In both cases the efficiency is about 92% for the first sub-target.

The efficiencies as a function of E_T can be deduced by means of the measured correlations between E_T and E_{ZDC}. They are plotted in Fig. 12 for the full (eff_{1-7}) and individual (eff_i) sub-targets.

5 Signature of projectile fragment interactions

5.1 Goal and method

The heavy projectile fragments and/or the light particles emitted around 0° are candidates for secondary interaction with production of light particles. The fragmentation mechanism is rather well known at 1-2 GeV/nucleon [11]. This is not the case for 100-200 GeV/nucleon. At these high energies, electromagnetic dissociation of the projectile spectator due to the high Coulomb field of the Pb nuclei could be important. Therefore, the term "projectile fragments" means indifferently nuclei and/or groups of nucleons. Anyhow, this secondary production constitutes a possible source of bias for information characterizing the primary collision. For example, a lack of energy in the zero degree calorimeter should be observed. Those effects, particularly visible at low E_{ZDC}, are magnified when the target thickness increases. It is therefore necessary to recognize such events, at least the most affected ones, in order to eliminate them and to make the experimental results independent of target thickness.

We define, for each event, the parameter q_j (e.g. Fig. 6 for $j = 2$) as the projection on the correlation axis of the measured quantity $[(\text{left } s_j)^2+(\text{right } s_j)^2]^{\frac{1}{2}}$. The method for detecting the interacting fragments is based on the comparison of this quantity q_j, from the vertex slats (q_{vn}) up to the last slats (q_7), with the corresponding average measured signals. The latter are defined for each identified vertex (vn), by the (8-vn) correlations (q_{vn}, $q_{j>vn}$) where q_{vn} is discretized under k channels of width Δq_{vn}. For each vertex number vn, a set of slat signal mean values ($m_{j,k}$ for $j = vn \rightarrow 7$) and standard deviation values ($\sigma_{j,k}$ for $j = vn \rightarrow 7$) are calculated after a few iterations in order to

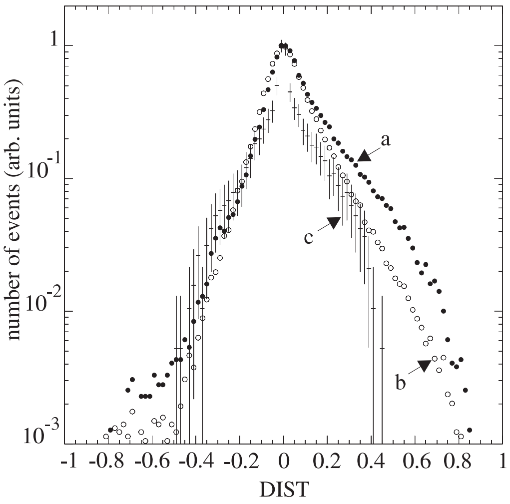

Fig. 13. Experimental DIST distributions for dimuon triggered Pb-Pb interactions in sub-target 1 (1 mm thickness) followed by a) 11 mm of lead, b) 6 mm of lead, c) no matter. See text Section 5.1.

eliminate the contribution of events too far from the mean value calculated in the preceding step. The difference between the current and the average slat pattern is evaluated by the relation [8]:

$$DIST = \frac{1}{8-vn}\sum_{j=vn}^{7}\{1-\exp-[\frac{q_{j,k}-m_{j,k}}{2\sigma_{j,k}}]^2\}\frac{|q_{j,k}-m_{j,k}|}{q_{j,k}-m_{j,k}}$$

which gives a value between -1 and 1 independent of the vertex number. The events without reinteractions are distributed symmetrically around 0. On the other hand, events with a reinteraction lie between 0 and 1.

5.2 Results

Distributions of the above quantity are shown in Fig. 13. In order to enhance the reinteraction effect, only events originating from sub-target 1 (vn = 1) are retained. The DIST functions calculated from experimental data collected with the 6 downstream sub-targets totalizing 6 or 11 mm of lead are plotted. As a comparison, we plotted in the same figure the DIST distribution given by experimental data with no sub-target downstream of sub-target 1.

The DIST distribution given by events from sub-target 1 without downstream sub-target is symmetrical around 0 and has a width which results exclusively from fluctuations of the slat signals. The distribution covers the full range from about -0.4 to 0.4. As expected, no evidence of reinteractions is visible in the right part of the distribution. In contrast, with sub-targets downstream

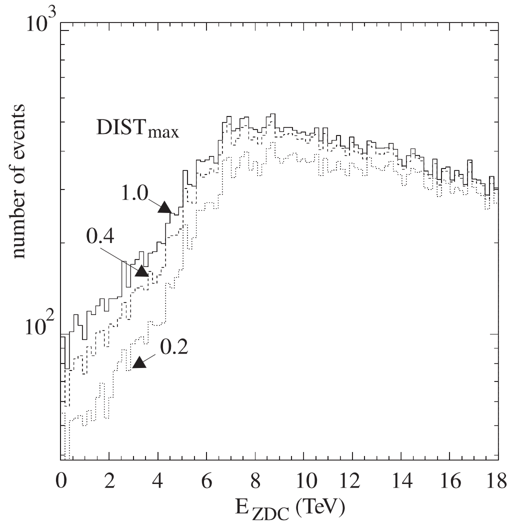

Fig. 14. Dimuon triggered Pb-Pb interactions in sub-target 1 (1 mm thickness) followed by 6 sub-targets totalizing 11 mm of lead. E_{ZDC} distributions as a function of the parameter $DIST_{max}$. See text Section 5.2.

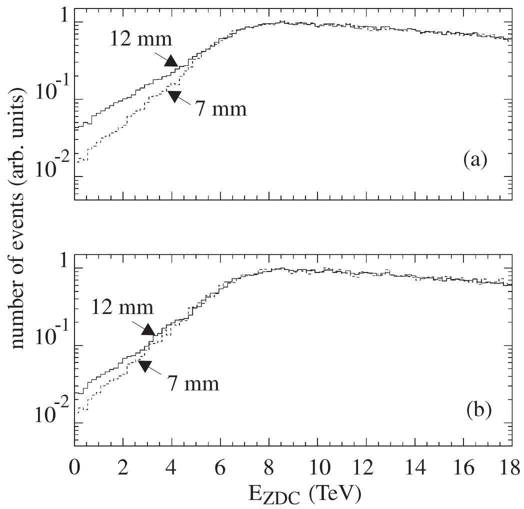

Fig. 15. Dimuon triggered Pb-Pb interactions in 7 sub-targets totalizing 7 mm and 12 mm thickness of lead. E_{ZDC} distributions with a) $DIST_{max} = 1$ (raw data), b) $DIST_{max} = 0.4$. See text Section 5.2.

from sub-target 1, while the negative part of the distributions remains nearly identical to the former one, an excess at positive DIST values is associated with fragment interactions. The greater the total thickness, the larger the effect. A DIST value between 0 and 0.4 indicates a mixture of events with and without reinteractions, while a DIST value larger than 0.4 indicates mainly events with a reinteraction. Obviously, such a representation does not allow to isolate every event with reinteraction. Nevertheless, the greater the reinteraction effect, the greater the DIST parameter. Therefore a suitable DIST threshold value will eliminate violent interactions of large fragment. A threshold value of 0.4 was chosen in order to eliminate exclusively reinteraction events.

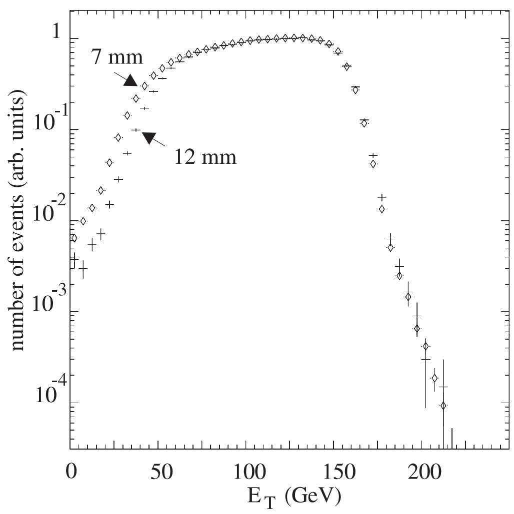

Fig. 16. Dimuon triggered Pb-Pb interactions in 7 sub-target totalizing 7 mm and 12 mm thickness of lead. E_T distributions with $DIST_{max} = 0.4$. See text Section 5.2.

The effect of the $DIST_{max}$ threshold from 1 (raw data) to 0.4 is shown in Fig. 14 on the low part of the E_{ZDC} distribution obtained from collisions in sub-target 1 followed by the thick sub-target set-up (distribution a in Fig. 13). It eliminates about 5.7% of the sub-target 1 statistics within the energy range 0-18 TeV. The same cut applied to the thin downstream sub-target set-up (distribution b in Fig. 13) leads to a statistics reduction of about 2.9%. The effect of a cut at 0.2 is also illustrated in Fig. 14.

Comparison of the full E_{ZDC} distributions (normalized at 9 TeV) recorded from the two set-ups (7 sub-targets totalizing 12 and 7 mm of lead) is shown in Fig. 15 for $DIST_{max}$ values 1 and 0.4. The raw distributions (Fig. 15a) present large differences at low E_{ZDC} due to the reinteractions. The cleaning effect of the $DIST_{max} = 0.4$ cut is clearly visible (Fig. 15b) on the distributions at low values. The reduction factor due to the cut, lower than if measured in the case of sub-target 1 events only, is about 2.1% and 1.1% for the two set-ups within the energy range 0-18 TeV. The distributions become much closer to each other and largely independent of the target thickness. In other words, thick subtargets can be used (for the benefit of the statistics) despite an increasing fragment interaction probability. The good quality of the measurement is still ensured.

A similar study can be done with the E_T distributions. The result is shown in Fig. 16 for the two target set-ups and the $DIST_{max}$ values 0.4. As already mentioned, the target efficiency difference between the two set-ups affects the low E_T part of the distributions. By contrast, the distributions are very similar at large E_T with $DIST_{max} = 0.4$, which confirms the cleaning effect of the procedure shown above from the E_{ZDC} distribution study. This algorithm with such cut is usually applied in the NA50 data analysis.

In summary, this study shows that it is possible to identify events with fragment interactions and to eliminate them from the recorded data. Thick subtargets can be used without excessive distortion of the recorded physical information.

6 Conclusion

The NA50 segmented target and vertex recognition system is made of seven sub-targets surrounded by quartz elements producing Čerenkov light. It is used to measure the dimuon production from the 158 GeV/nucleon ^{208}Pb-Pb collisions at the CERN-SPS. Its segmented configuration prevents against the harmful effects of the secondary light particle interactions in the surrounding matter.

The geometrical optimisation of this device and a simple algorithm lead to a vertex recognition efficiency better than 85% for the seven 1 mm sub-target arrangement, and of about 92% for the first sub-target, with a loss of performance at large forward residual energy (at low transverse energy).

A search for projectile fragment interactions is based on a pattern analysis of the counter responses. It allows to eliminate dimuon events for which correlated quantities such as the remaining forward energy and the transverse energy are corrupted. These events represent about 5.7% and 2.9% (within the E_{ZDC} range 0-18 TeV) of the events originating from the first sub-target followed by 11 mm and 6 mm of lead segmented in 6 sub-targets. These percentages become 2.1% and 1.1% with full statistics (vertex in any sub-target).

This successful identification of reinteractions allows to use thick targets with the ensurance of clean measurements. Associated to a high intensity ion beam ($\approx 10^7$ ions/s), high statistics dimuon collection can be achieved. The 1995 data taking have been performed with a 7 mm thick target ($\approx$17.5% of interaction length). The 1996 data have been taken with twice as much luminosity, precisely 12 mm of target thickness representing $\approx$30% of interaction length.

Acknowledgement

The authors would like to express their thanks to the CERN Experimental Areas (EA) group for their high level support during the set up of the equipment. They appreciated the help of L. Gatignon for the beam control and adjustment. The authors are also indebted to the work of many people, particularly, D. Essertaize for the mechanics studies, the workshop team of the Institut de Physique Nucléaire de Lyon for the mechanics construction, G. Jacquet and M. Alexeline for the monitoring and data acquisition software of the segmented target. Lastly, this work could not be carried out without the numerous contributions by the NA50 collaborators. The authors are very grateful to them all.

References

[1] NA38 Collaboration, Phys. Lett. B 220 (1989) 471.

[2] NA38 Collaboration, Phys. Lett. B 251 (1990) 465; B 251 (1990) 472; B 255 (1991) 459; B 262 (1991) 362; B 268 (1991) 453.

[3] NA38 Collaboration, Phys. Lett. B 270 (1991) 105.

[4] M.C. Abreu et al., Study of muon pairs and vector mesons produced in high energy Pb-Pb interactions, Report CERN/SPSLC 91-55, Proposal SPSLC/P 265-Rev.

[5] NA10 Collaboration, Nucl. Instr. Meth. Phys. Res. 223 (1984) 26.

[6] B. Alessandro et al., Nucl. Instr. Meth. Phys. Res. A360 (1995) 189.

[7] O.M. Alimi, Thesis, Université de Lyon, 1988.

[8] F. Bellaiche, Thesis, Université de Lyon, 1997.

[9] B. Nilsson-Almqvist and E. Stenlund, Comp. Phys. Comm. 43 (1987) 387; FRITIOF version 7.

[10] R. Brun et al., GEANT 3, CERN program library Q123.

[11] H.H. Heckman et al., Phys. Rev. Lett. 28 (1972) 926.
P.J. Lindstrom et al., Lawrence Berkeley Laboratory, Report LBL-3650 (1975).
D.E. Greiner et al., Phys. Rev. Lett. 35 (1975) 152.
G.D. Westfall et al., Phys. Rev. C19 (1979) 1309.
D.L. Olson et al., Phys. Rev. C24 (1981) 1529.